Three-Dimensional DDA and DLSM Coupled Approach for Rock Cutting and Rock Penetration

Gao-Feng Zhao[1]; Ji-Jian Lian[2]; Adrian R. Russell[3]; and Jian Zhao[4]

Abstract: Rock cutting and rock penetration are typical problems in civil, mining, petroleum, and geothermal engineering disciplines. They involve dynamic fracturing and fragmentation of rock, high-speed movements of a cutter/impactor, and complex dynamic contacts between the cutter/impactor and the rock. In this study a new three-dimensional (3D) coupled approach is developed to address these problems. The distinct lattice spring model (DLSM) is used to simulate the dynamic fracturing process of the rock, and the discontinuous deformation analysis (DDA) is adopted to model the high-speed motion of the cutter/impactor. An explicit-implicit coupling scheme is developed to bridge DLSM and DDA. Moreover, to take account of interaction between DLSM and DDA, a 3D simplex sphere-to-block contact method is introduced. Finally, a number of numerical examples are conducted to verify the implementation of the coupled approach and its ability to model rock cutting and rock penetration problems. **DOI: 10.1061/(ASCE)GM.1943-5622.0000754.**

Author keywords: Discontinuous deformation analysis (DDA); Distinct lattice spring model (DLSM); Rock cutting; Rock penetration.

Introduction

Rock cutting and rock penetration involve dynamic fracturing of rock, high-speed motion of the cutter/impactor, and complex interaction between the cutter/impactor and the rock. There are three available approaches to study these problems: experimental (Kaitkay and Lei 2005; Glowka 1989; Yin et al. 2014), analytical (Nishimatsu 1972; Detournay et al. 2008; Hughes 1984; Li and Chen 2003; Li et al. 2008), and numerical (Liu et al. 2002; Cho et al. 2010; Ma et al. 2011). The experimental approach can provide physical insights into the behavior of rock cutting and rock penetration. However, due to the expense and time involved in model construction, it is usually impracticable to conduct many tests and assess sensitivity of behavior to model and rock parameters. Moreover, to perform these tests under laboratory conditions, some specifications, e.g., the size of rock model specimen and the geometry of the loading device, have to be simplified and scaled, which may introduce uncertainties in how the results apply to real problems. These limitations constrained the experimental approaches to be used for research rather than a predictive tool of guiding the actual rock cutting/penetration operation. Analytical models can provide useful insights into the relationship between basic rock mechanical parameters (e.g., elastic modulus and compressive strength) and the final cutting/penetration results (e.g., cutting volume/penetration depth). Nevertheless, these analytical equations can only be derived under simplified loading conditions and usually ignore the nonlinear stress-strain relationship, rock heterogeneity, and dynamic failure processes. With improvement of modern computers and computing power, numerical modeling techniques provide a very promising solution to the study of rock cutting and penetration because they do not suffer from the same limitations as the experimental and analytical approaches.

Many numerical methods, e.g., the FEM, the boundary element method (BEM), the discrete element method (DEM), and the smoothed particle hydrodynamics (SPH), have been applied to study rock cutting and/or rock penetration problems (Table 1). These methods can be classified as either continuum-based methods or discontinuum-based methods (Jing 2003). For most continuum-based methods failure of rock is modeled using the element/particle degradation technique (Hansson and Skoglund 2002; Gong et al. 2006; Cho et al. 2010; Ma et al. 2011) or the crack growth technique based on linear fracture mechanics (Guo 1990; Ingraffea 1987). The cutter/impactor is treated as a boundary condition or another FEM model. Interaction between the rock and the cutter/impactor is handled by sharing common nodes (Ma et al. 2011) or contact treatment between the rock and the cutter/impactor (Cho et al. 2010). The main shortcoming of the continuum-based approach is its unsuitability for dealing with complete detachment and large-scale fracture opening during postfailure of the rock. Conversely the discontinuum-based method is good at simulating the complex mechanical responses of the rock during fracturing and fragmentation (Kusano et al. 1992; Moon and Oh 2012). In the discontinuum-based approach the cutter/impactor is usually treated as another DEM model, a wall element, or a clumped particle. Interaction between the cutter/impactor and the rock is handled as a contact problem. Treating the cutter/impactor as a DEM model is realistic; however, the computational cost is usually very high. Using the wall element can overcome this shortcoming. Nevertheless, it can only apply to velocity loading and is unable to consider the kinematic interaction between the rock and the cutter/impactor. The particle clumping technique is a compromise solution in which a group of particles [sharing the same degrees of freedom (DOFs)] are attached and represent the cutter/impactor. One major shortcoming

[1]Professor, State Key Laboratory of Hydraulic Engineering Simulation and Safety, School of Civil Engineering, Tianjin Univ., Tianjin 300072, China (corresponding author). E-mail: gaofeng.zhao@tju.edu.cn

[2]Professor, State Key Laboratory of Hydraulic Engineering Simulation and Safety, School of Civil Engineering, Tianjin Univ., Tianjin 300072, China.

[3]Associate Professor, Centre for Infrastructure Engineering and Safety, School of Civil and Environmental Engineering, Univ. of New South Wales, Sydney, NSW 2052, Australia.

[4]Professor, Dept. of Civil Engineering, Monash Univ., Building 60, Clayton, VIC 3800, Australia.

Note. This manuscript was submitted on November 20, 2015; approved on June 7, 2016; published online on August 17, 2016. Discussion period open until January 17, 2017; separate discussions must be submitted for individual papers. This paper is part of the ***International Journal of Geomechanics***, © ASCE, ISSN 1532-3641.

Table 1. Numerical Methods Used for Rock Cutting and Rock Penetration Problems

Literature	Topic	Method	Dimension	Modeling technique		
				Rock	Interaction	Cutter/impactor
Ingraffea (1987)	Cutting	FEM (implicit)	2	Fracture mechanics	Common node	FEM
Guo (1990)	Cutting	BEM (implicit)	2	Fracture mechanics	None	Boundary condition
Kusano et al. (1992)	Penetration	DEM (explicit)	2	Bond failure	Contact	DEM
Liu et al. (2002)	Cutting	FEM (implicit)	2	Element degradation	Common node	FEM
Hansson and Skoglund (2002)	Penetration	SPH (explicit)	2	Particle degradation	Contact	FEM
Onate and Rojek (2004)	Cutting and penetration	DEM-FEM (explicit)	3	Bond failure	Contact	FEM
Gong et al. (2006)	Cutting	DEM-FDM (explicit)	2		None	Boundary condition
Zhou (2009)	Penetration	DEM (explicit)	3	Bond failure	Contact	DEM (clump particle)
Shiu et al. (2009)	Penetration	DEM (explicit)	3	Bond failure	Contact	DEM (clump particle)
Cho et al. (2010)	Cutting	FEM (explicit)	3	Element degradation	Contact	FEM
Ma et al. (2011)	Cutting	FEM (implicit)	2	Element degradation	Common node	FEM
Moon and Oh (2012)	Cutting	DEM (explicit)	2	Bond failure	Contact	Wall element
Zhou (2013)	Cutting	FEM (explicit)	3	Element degradation	Contact	FEM

of the discontinuum-based approach is a proper calibration of the micromechanics parameters required to obtain reasonable results. A coupled discontinuum-continuum approach takes advantage of the continuum-based and discontinuum-based methods while avoiding these shortcomings (Munjiza 2004; Mahabadi et al. 2012). For rock cutting and penetration problems other coupled approaches have also been developed (Onate and Rojek 2004) in which the rock is simulated using the DEM, and the cutter/impactor is treated as a FEM. In the coupled FEM/DEM approach (Onate and Rojek 2004) both the FEM and DEM are solved explicitly. The coupling between the FEM and DEM is realized through the contact between particles (DEM) and the three-dimensional (3D) cutter/impactor (FEM). Implementing this coupled FEM/DEM approach into a computer code usually requires complex routines. Moreover, treating the cutter/impactor as a 3D FEM model is computationally costly due to many extra DOFs needed for a realistic 3D cutter/impactor. Because an explicit solution is used for the FEM model, the time step of the coupled model is also influenced by the mesh size and elastic parameters of the cutter/impactor. For some cases, e.g., rock cutting with a very rigid cutter, the time step has to be very small to guarantee numerical stability of the cutter adding to the computational inefficiency.

In this work a new coupled approach is developed in which the rock is handled using the distinct lattice spring model (DLSM) (Zhao et al. 2011). The reasons for selecting DLSM as the discontinuum-based part are (1) it can directly use macroscopic parameters without requiring the calibration process, (2) it uses only half of the DOFs compared with DEM, and (3) parallelization of the algorithm is relatively simple (Zhao et al. 2013). The discontinuous deformation analysis (DDA) (Shi 1988; Shi and Goodman 1985) is adopted to model the cutter/impactor, which provides advantages through its large deformation capability and its suitability to accommodate large time steps. Because both 3D DDA (Jiang and Yeung 2004; Yeung et al. 2007) and DLSM have been well developed theoretically, the main contribution of this work is to couple them and solve a range of rock cutting and penetration problems. Three techniques are developed further in this paper: (1) the simplex representation of the cutter/impactor as a group of 3D triangles, (2) a simplex 3D particle-block contact treatment, and (3) an explicit-implicit coupling scheme to integrate DLSM (explicit) and DDA (implicit). The paper is organized as follows. First, the basic principle of DLSM is described. Then formulations of 3D DDA adopted in this work are presented. Next the coupling techniques are introduced. Finally, a newly developed DDA-DLSM is demonstrated through a number of numerical examples.

The Model

DLSM

As shown in Fig. 1(a), in DLSM the rock is represented as a group of mass particles linked by spring bonds made up of normal and shear springs. The rock fracturing and failure process is controlled by bond failure described from the corresponding constitutive model for these springs [see Fig. 1(b)]. In model preparation, spring bonds are formed when the gap between two particles is smaller than a prescribed threshold value. The system equation of DLSM is given as

$$[\mathbf{K}]\mathbf{d} + [\mathbf{C}]\dot{\mathbf{d}} + [\mathbf{M}]\ddot{\mathbf{d}} = \mathbf{F}(t) \tag{1}$$

where $\mathbf{d}$ = particle displacement; $\dot{\mathbf{d}}$ = particle velocity; $\ddot{\mathbf{d}}$ = particle acceleration; $[\mathbf{K}]$ = stiffness matrix; $[\mathbf{M}]$ = lumped mass matrix; $[\mathbf{C}]$ = damping matrix; and $\mathbf{F}(t)$ = external force. The explicit central finite-difference scheme is adopted to solve Eq. (1).

The calculation cycle of DLSM is as follows. First, update the particle positions from the prescribed displacements or calculated displacements from the previous step. Given the updated particle displacements, new contacts and broken bonds are detected. Following this, the particle forces are calculated from spring bonds and contacts according to the force-displacement relationship as shown in Fig. 1(b). Finally, the particle velocity is updated as

$$\dot{\mathbf{d}}_i^{(t+\Delta t/2)} = \dot{\mathbf{d}}_i^{(t-\Delta t/2)} + \frac{\sum \mathbf{F}_j^{(t)}}{m_p}\Delta t \tag{2}$$

where $\dot{\mathbf{d}}_i^{(t+\Delta t/2)}$ presents the particle velocity at $t + \Delta t/2$; $\dot{\mathbf{d}}_i^{(t-\Delta t/2)}$ presents the particle velocity at $t - \Delta t/2$; m_p = particle mass, $\sum \mathbf{F}_j^{(t)}$ = sum of contact forces acting on the particle i including external forces from boundary conditions and gravity; and Δt is the time step. Finally, the particle displacements are obtained as

$$\mathbf{d}_i^{(t+\Delta t)} = \mathbf{d}_i^{(t)} + \dot{\mathbf{d}}_i^{(t+\Delta t/2)}\Delta t \tag{3}$$

where $\mathbf{d}_i^{(t+\Delta t)}$ is the particle displacement at $t + \Delta t$; $\dot{\mathbf{d}}_i^{(t+\Delta t/2)}$ is the particle velocity at $t + \Delta t/2$; and $\mathbf{d}_i^{(t)}$ is the particle displacement at t.

The relative displacement of a bond connecting particle i and particle j is written as

$$\mathbf{d}_{ij} = \mathbf{d}_j - \mathbf{d}_i \tag{4}$$

When the normal unit vector of the bond pointing from particle i to particle j is defined as $\mathbf{n} = (n_x, n_y, n_z)^T$ then the normal force of the bond is

$$\mathbf{F}_{ij}^n = k_n(\mathbf{d}_{ij} \cdot \mathbf{n})\mathbf{n} \tag{5}$$

where k_n = stiffness of the normal spring. In DLSM, a multibody shear spring was introduced to address the noncentral interaction arising from the bond's shear deformation

$$\hat{\mathbf{d}}_{ij}^s = [\bar{\boldsymbol{\varepsilon}}]_{\text{bond}}\mathbf{n}l - (([\bar{\boldsymbol{\varepsilon}}]_{\text{bond}}\mathbf{n}l) \cdot \mathbf{n})\mathbf{n} \tag{6}$$

where $[\bar{\varepsilon}]_{\text{bond}} = [\bar{\varepsilon}]_i + [\bar{\varepsilon}]_j/2$ is the local approximated strain of the bond; and $[\bar{\varepsilon}]_i$ and $[\bar{\varepsilon}]_j$ = local approximated strains at the two particles. The local approximated strains of the particles are calculated from particle displacements within a particle cluster using a least-squares method. Given the shear displacement the corresponding shear force is

$$\mathbf{F}_{ij}^s = k_s\hat{\mathbf{d}}_{ij}^s \tag{7}$$

where k_s = stiffness of the shear spring.

To solve static problems by DLSM, mechanical damping is adopted for which Eq. (2) becomes

$$\dot{\mathbf{d}}_i^{(t+\Delta t/2)} = \dot{\mathbf{d}}_i^{(t-\Delta t/2)} + \left\{\sum \mathbf{F}_j^{(t)} - c_\alpha\left|\sum \mathbf{F}_j^{(t)}\right|\text{sgn}\left(\dot{\mathbf{d}}_i^{(t-\Delta t/2)}\right)\right\}\frac{\Delta t}{m_p} \tag{8}$$

where c_α = damping constant (with a default value of 0.8).

Eqs. (1)–(8) make up the main framework of DLSM. More details on implementation and verification of DLSM can be found in Zhao et al. (2011).

DDA

The DDA (Shi 1988; Shi and Goodman 1985) is an implicit DEM. There are four essential components of DDA: (1) a deformation function of the block, (2) contact detection between blocks, (3) a system equation derived from an energy minimization principle, and (4) simplex integration. In this work the cutter/impactor is represented as a tessellation of surface triangles using the simplex concept of DDA (Fig. 2). Representing a solid as a tessellation of triangles is a classical method used in computer graphics, e.g., the stereo lithography (STL) file for formatting and recording 3D objects in computer science. In this work the tessellated triangle surface is extracted from a 3D FEM model. The normal direction of each triangle is outside of the domain (see Fig. 2). The deformation of the block is represented as

$$\begin{pmatrix} u \\ v \\ w \end{pmatrix} = [\mathbf{T}]\mathbf{D} \tag{9}$$

where $[\mathbf{T}]$ = deformation matrix of the block; and $\mathbf{D}$ = general DOFs.

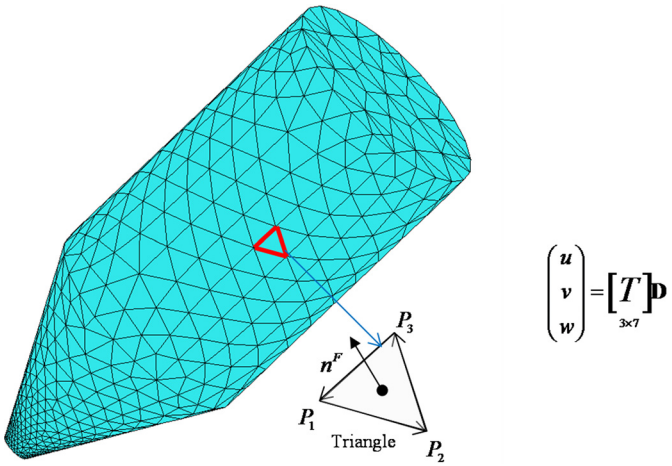

Fig. 2. Representation of a 3D object as triangles in 3D DDA

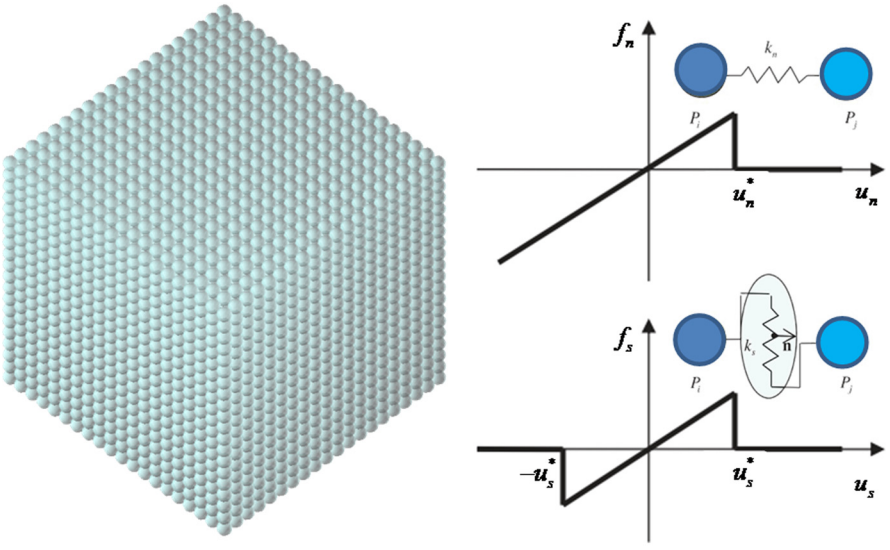

(a) (b)

Fig. 1. Computational model and constitutive model of DLSM (data from Zhao et al. 2011): (a) particle model; (b) constitutive model

Theoretically a displacement function of any order can be used to approximate the block's deformation (Beyabanaki et al. 2010). The corresponding DOFs are made up from the translation displacement, rotation, simple strain, and other high-order terms. In this work, because rock fracturing is the main concern, the DDA block's deformation is assumed to be ignorable due to its high rigidity; therefore, the deformation function of the DDA block can be simplified as the incomplete first-order displacement function used in sphere-based DDA (Zhao 2000; Beyabanaki and Bagtzoglou 2015)

$$\begin{pmatrix} u \\ v \\ w \end{pmatrix} = [\mathbf{T}(x,y,z)]\mathbf{D} = \begin{bmatrix} 1 & 0 & 0 & 0 & Z & -Y & X \\ 0 & 1 & 0 & -Z & 0 & X & Y \\ 0 & 0 & 1 & Y & -X & 0 & Z \end{bmatrix} \begin{pmatrix} d_x \\ d_y \\ d_z \\ r_x \\ r_y \\ r_z \\ \varepsilon_r \end{pmatrix} \tag{10}$$

where $(X, Y, Z) = (x - x_c, y - y_c, z - z_c)$; (x_c, y_c, z_c) = centroid of the block; d_x = translation in x direction; r_x = rotation along x-axis (terms for y and z defined similarly); and ε_r = radius strain deformation.

From Eq. (10) the elastic potential in the block can be calculated as

$$\Pi^e = \iiint \frac{1}{2} \begin{pmatrix} \varepsilon_r & \varepsilon_r & \varepsilon_r \end{pmatrix} \frac{E}{1-2\nu} \begin{pmatrix} \varepsilon_r \\ \varepsilon_r \\ \varepsilon_r \end{pmatrix} dxdydz = \iiint \frac{1}{2} \varepsilon_r \frac{3E}{1-2\nu} \varepsilon_r dxdydz = \frac{1}{2} V \varepsilon_r \frac{3E}{1-2\nu} \varepsilon_r = \frac{V}{2} \mathbf{D}^T [\mathbf{E}] \mathbf{D} \tag{11}$$

where

$$[\mathbf{E}] = \begin{bmatrix} 0 & 0 & 0 & 0 & 0 & 0 & 0 \\ 0 & 0 & 0 & 0 & 0 & 0 & 0 \\ 0 & 0 & 0 & 0 & 0 & 0 & 0 \\ 0 & 0 & 0 & 0 & 0 & 0 & 0 \\ 0 & 0 & 0 & 0 & 0 & 0 & 0 \\ 0 & 0 & 0 & 0 & 0 & 0 & 0 \\ 0 & 0 & 0 & 0 & 0 & 0 & \dfrac{3E}{1-2\nu} \end{bmatrix}$$

The block stiffness matrix is obtained using the energy minimization principle as

$$[\mathbf{K}_b] = \begin{bmatrix} 0 & 0 & 0 & 0 & 0 & 0 & 0 \\ 0 & 0 & 0 & 0 & 0 & 0 & 0 \\ 0 & 0 & 0 & 0 & 0 & 0 & 0 \\ 0 & 0 & 0 & 0 & 0 & 0 & 0 \\ 0 & 0 & 0 & 0 & 0 & 0 & 0 \\ 0 & 0 & 0 & 0 & 0 & 0 & 0 \\ 0 & 0 & 0 & 0 & 0 & 0 & \dfrac{3VE}{1-2\nu} \end{bmatrix} \tag{12}$$

where V = volume of the block, which is calculated using the 3D simplex integration method; E = elastic modulus of the block; and ν is Poisson's ratio.

For a time step $(0, \Delta t)$, where $0 \le t \le \Delta t$, and for $[\mathbf{D}(0)] = [0]$, $[\mathbf{D}(\Delta t)] = [\mathbf{D}]$, the inertial force can be obtained as

$$\begin{pmatrix} f_x \\ f_y \\ f_z \end{pmatrix} = -\rho \begin{pmatrix} \frac{\partial^2}{\partial t^2} u(t) \\ \frac{\partial^2}{\partial t^2} v(t) \\ \frac{\partial^2}{\partial t^2} w(t) \end{pmatrix} = -\rho [\mathbf{T}(x,y,z)] \left[\frac{\partial^2}{\partial t^2} \mathbf{D}(t) \right] \tag{13}$$

Applying Taylor expansion to $[\mathbf{D}(0 + \Delta t)]$ gives

$$[\mathbf{D}(0+\Delta t)] = [\mathbf{D}(0)] + \frac{\Delta t}{1!} \frac{\partial}{\partial t} [\mathbf{D}(t)]\Big|_{t=0} + \frac{\Delta t^2}{2!} \frac{\partial^2}{\partial t^2} [\mathbf{D}(t)]\Big|_{t=0} \tag{14}$$

where $\frac{\partial}{\partial t} [\mathbf{D}(t)]\Big|_{t=0} = [\dot{\mathbf{D}}(0)]$ is the initial velocity. Because

$$[\mathbf{D}] = \Delta t [\dot{\mathbf{D}}(0)] + \frac{\Delta t^2}{2!} \frac{\partial^2}{\partial t^2} [\mathbf{D}(t)]\Big|_{t=0} \tag{15}$$

it follows that

$$\frac{\partial^2}{\partial t^2} [\mathbf{D}(t)]\Big|_{t=0} = \frac{2}{\Delta t^2} [\mathbf{D}] - \frac{2}{\Delta t} [\dot{\mathbf{D}}(0)] \tag{16}$$

The inertial energy of the block is written as

$$\Pi^i = \iiint \rho [\mathbf{D}]^T [\mathbf{T}(x,y,z)] \frac{\partial^2}{\partial t^2} [\mathbf{D}] dxdydz \tag{17}$$

where ρ = density of the block. The inertial matrix and inertial forces can be obtained using the energy minimization principle as

$$[\mathbf{K}_{\text{in}}] = \frac{2\rho}{\Delta t^2} \iiint [\mathbf{T}(\mathbf{x},\mathbf{y},\mathbf{z})]^T [\mathbf{T}(\mathbf{x},\mathbf{y},\mathbf{z})] dxdydz \tag{18}$$

$$[\mathbf{F}_{\text{in}}] = -\rho \iiint [\mathbf{T}(\mathbf{x},\mathbf{y},\mathbf{z})]^T [\mathbf{T}(\mathbf{x},\mathbf{y},\mathbf{z})] dxdydz \left(\frac{2}{\Delta t^2} [D_i] - \frac{2}{\Delta t} [\dot{D}_i(0)] \right) \tag{19}$$

The equation of point loading applied to the block is

$$[\mathbf{F}_f] = [\mathbf{T}(x,y,z)] \begin{pmatrix} f_x \\ f_y \\ f_z \end{pmatrix} \tag{20}$$

where (f_x, f_y, f_z) is a concentrated force (either a contact force from the rock or an external force) applied at a point (x, y, z) of the block.

Equations for a fixed point are

$$[\mathbf{F}_{\text{fix}}] = p[\mathbf{T}(x,y,z)]^T \begin{pmatrix} u_0 \\ v_0 \\ w_0 \end{pmatrix} \tag{21}$$

$$[\mathbf{K}_{\text{fix}}] = p[\mathbf{T}(x,y,z)]^T[\mathbf{T}(x,y,z)] \tag{22}$$

where p = penalty number that is calculated as βE (with $\beta = 40$ used in this study).

The gravity force can be calculated as

$$[\mathbf{F}_g] = \rho V \begin{pmatrix} g_x \\ g_y \\ g_z \end{pmatrix} \tag{23}$$

where (g_x, g_y, g_x) is the acceleration of gravity applied to the model.

Assembling these equations produces the system equation written as

$$([\mathbf{K}_b] + [\mathbf{K}_{\text{in}}] + \sum[\mathbf{K}_{\text{fix}}])[D] = [\mathbf{F}_{\text{in}}] + [\mathbf{F}_g] + \sum[\mathbf{F}_f] + \sum[\mathbf{F}_{\text{fix}}] \tag{24}$$

The block movement $[D]$ can be obtained by solving the Eq. (24). The 3D integration operation in Eqs. (18) and (19) is performed using the simplex integration. Details on the original simplex integration can be found in the work of Shi (1988) and Jiang et al. (2009). Here a set of equations specially developed for the triangle tessellated DDA block are derived.

Simplex integration is one of the most distinct characteristics of DDA. *Divide and conquer* is the fundamental principle of simplex integration. There are two levels of division, (1) an algebraic layer and (2) a geometric level. In the algebraic layer the integration of a general polynomial function is performed as

$$\iiint_{\Omega} f(x,y,z)d\Omega = \sum \iiint_{\Omega} C_i x^m y^n z^l d\Omega \tag{25}$$

Unlike the Gauss integration, the simplex integration tries to calculate the analytical integration of each polynomial component separately. At the geometric level the integration domain is further divided into a group of simplex domains (tetrahedron in 3D). The subdomain has its own sign according to its topological condition. In this work the block was represented as subdomains that are made up from the surface triangles and the origin of coordinates (Fig. 3). For each triangle $(x_i, y_i, z_i)_{i=1,2,3}$ its signed volume (see Fig. 3) is given as

$$V_s^i = \frac{-x_3y_2z_1 + x_2y_3z_1 + x_3y_1z_2 - x_1y_3z_2 - x_2y_1z_3 + x_1y_2z_3}{6} \tag{26}$$

According to the equations (after Shi 1988) the analytical integration of x, y, z, x^2, y^2, z^2, xy, xz, and yz in the subdomain can be further simplified as

$$s_x^i = \frac{(x_1 + x_2 + x_3)V_s^i}{4} \tag{27}$$

$$s_y^i = \frac{(y_1 + y_2 + y_3)V_s^i}{4} \tag{28}$$

$$s_z^i = \frac{(z_1 + z_2 + z_3)V_s^i}{4} \tag{29}$$

$$s_{x^2}^i = \frac{(x_1x_2 + x_1x_3 + x_2x_3 + x_1x_1 + x_2x_2 + x_3x_3)V_s^i}{20} \tag{30}$$

$$s_{y^2}^i = \frac{(y_1y_2 + y_1y_3 + y_2y_3 + y_1y_1 + y_2y_2 + y_3y_3)V_s^i}{20} \tag{31}$$

$$s_{z^2}^i = \frac{(z_1z_2 + z_1z_3 + z_2z_3 + z_1z_1 + z_2z_2 + z_3z_3)V_s^i}{20} \tag{32}$$

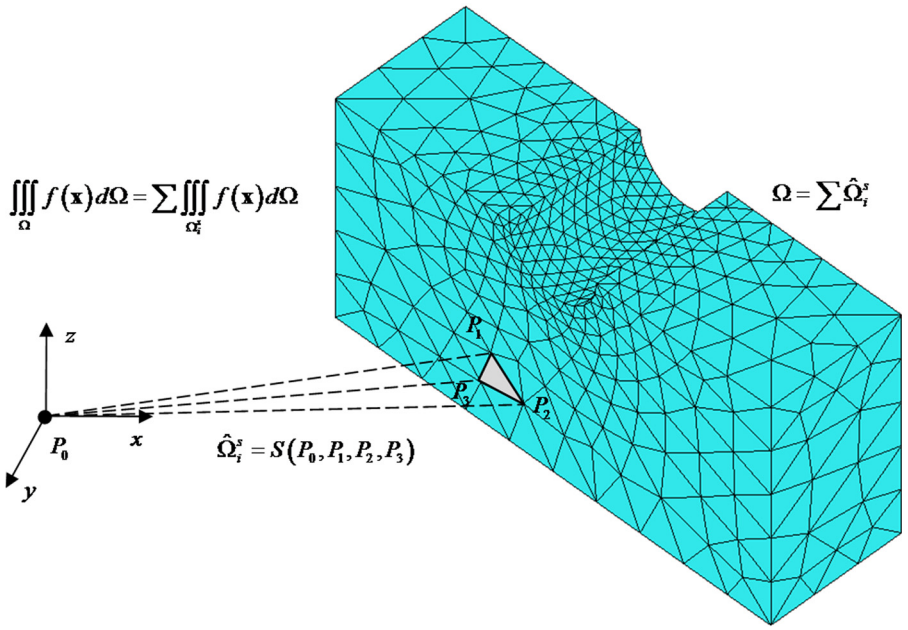

Fig. 3. Simplex integration scheme of 3D DDA

$$s_{xy}^i = \frac{(x_1y_2 + x_1y_3 + x_2y_3 + x_2y_1 + x_3y_1 + x_3y_2 + 2(x_1y_1 + x_2y_2 + x_3y_3))V_s^i}{20} \tag{33}$$

$$s_{xz}^i = \frac{(x_1z_2 + x_1z_3 + x_2z_3 + x_2z_1 + x_3z_1 + x_3z_2 + 2(x_1z_1 + x_2z_2 + x_3z_3))V_s^i}{20} \tag{34}$$

$$s_{yz}^i = \frac{(y_1z_2 + y_1z_3 + y_2z_3 + y_2z_1 + y_3z_1 + y_3z_2 + 2(y_1z_1 + y_2z_2 + y_3z_3))V_s^i}{20} \tag{35}$$

These equations enable simplex integration of a complete two-order function and are enough to calculate the integration operation in this work. Eqs. (26)–(35) can be easily implemented into a computer code.

Coupling between DDA and DLSM

Fig. 4 shows the process for coupling DDA and DLSM. Each calculation cycle includes two time lines: one is for DLSM to update a particle's motion according to Newton's second law, and the other is for DDA to calculate the block displacement according to the energy minimization principle. The coupling is realized through exchange contact forces between the DDA block and the particle model (see Fig. 4). More specifically, the influence the DDA block has on DLSM is considered as a contact force. For DDA calculation, according to Newton's third law, a reaction force is applied to the block at the contact point. Therefore the sphere-block contact is where the coupling is implemented. In this work the block is represented as a tessellation of triangles. Instead of the complex contact algorithm described in Beyabanaki and Bagtzoglou (2015) or He et al. (2014), a simplified version is adopted, which is where the concept of simplex integration is developed further. The principle is to divide the contact between particles and the block into elemental contacts between spheres and triangles (Fig. 5). The center of the sphere is represented as $\mathbf{P}_s$, and the triangle is described from three points $(\mathbf{P}_1, \mathbf{P}_2, \mathbf{P}_3)$. If there is a contact between a sphere and a triangle then its normal is denoted as $\mathbf{n}_c^{\text{sf}}$ and the overlap as d^{sf}. The stiffness of the normal spring linked to the particle is k_n, meaning the contact force from the block to the particle is given as

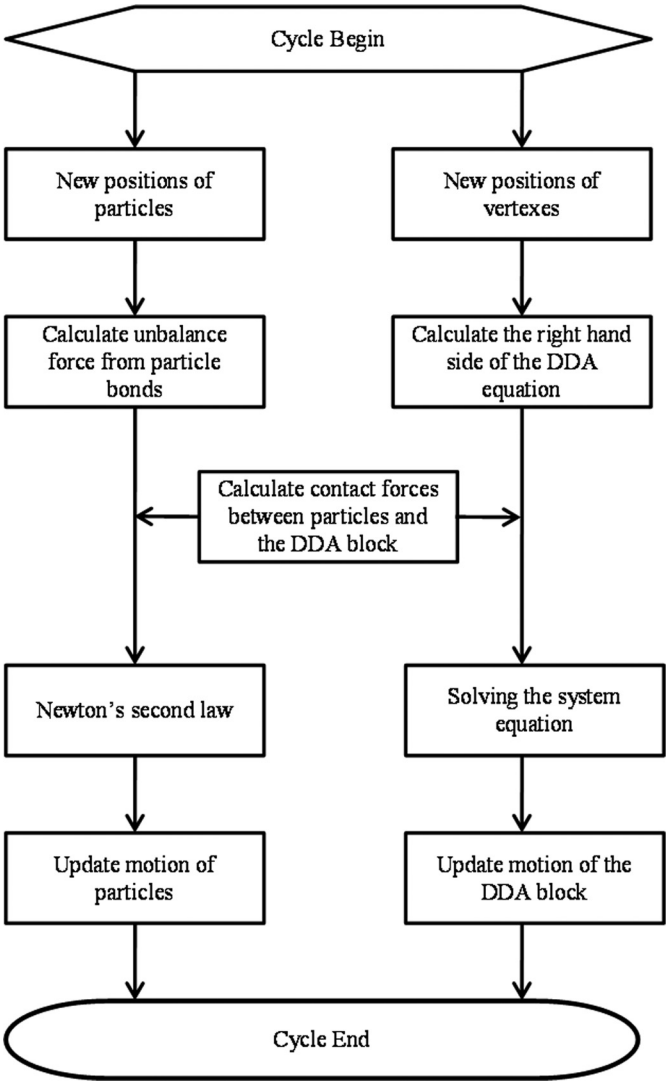

Fig. 4. Explicit-implicit coupling scheme of DDA and DLSM

$$\mathbf{F}^{\text{sf}} = \alpha 2k_n\mathbf{n}_c^{\text{sf}}d^{\text{sf}} \tag{36}$$

where α is a coefficient depending on the contact type. The purpose of α is to smooth the contact force when the sphere moves between triangles. When contact between a sphere and a triangle is viewed as contact area rather than a point, the contact stiffness should be related to the effective contact area. Under this principle, for a sphere-vertex (SV) contact, α is estimated as the ratio between the corresponding angle of the triangle's vertex θ_i [see Fig. 5(b)] and 2π

$$\alpha = \frac{\theta_i}{2\pi} \tag{37}$$

From a simple geometric analysis, for a sphere-edge (SE) contact and a sphere-face (SF) contact, α is 0.5 and 1.0, respectively. Additionally for SF contact there are two special conditions that need to be considered [see Fig. 5(b)]. When the contact point is too close to a vertex or an edge the contact coefficient needs to be modified as detailed next.

For a SF contact shown in Fig. 5(a) the first step is to calculate the distance between the triangle and the sphere's center using

$$b^{\text{FS}} = \overrightarrow{\mathbf{P}_1\mathbf{P}_s} \cdot \mathbf{n}^F \tag{38}$$

where $\mathbf{n}^F$ = normal vector of the triangle. The contact detection is performed only if $b^{\text{FS}} \geq 0$. A potential contact point $\mathbf{P}_4^{\text{SF}}$ is then obtained as

$$\mathbf{P}_4^{\text{SF}} = \mathbf{P}_s - \mathbf{n}^F b^{\text{FS}} \tag{39}$$

If $b^{\text{FS}} < R$ then the following step is used to judge whether the contact point falls inside the triangle:

$$\Delta(\mathbf{P}_1,\mathbf{P}_2,\mathbf{P}_3) = \Delta(\mathbf{P}_1,\mathbf{P}_2,\mathbf{P}_4^{\mathrm{SF}}) + \Delta(\mathbf{P}_2,\mathbf{P}_3,\mathbf{P}_4^{\mathrm{SF}}) + \Delta(\mathbf{P}_3,\mathbf{P}_1,\mathbf{P}_4^{\mathrm{SF}}) \tag{40}$$

where $\Delta(\cdot)$ represents the calculation of the area of a triangle made up from the three points inside (). If Eq. (40) is satisfied then the contact is a SF type and its contact direction is given as

$$\mathbf{n}_c^{\mathrm{sf}} = \mathbf{n}^F \tag{41}$$

The contact overlap is calculated as

$$d^{\mathrm{sf}} = R - b^{\mathrm{FS}} \tag{42}$$

For a SF contact the coefficient α needs to be further determined according to arrangements shown in Fig. 5(b). If the distance between a triangle vertex and the potential contact point is smaller than a threshold value $\delta^{\mathrm{SF}} = \beta R$ (in this work $\beta = 0.01$), then α will be assigned to the corresponding value for a SV contact of the triangle's vertex. The same procedure is applied for edges.

The SE contact type is considered when the contact does not satisfy conditions necessary for it to be a SF type. For the example of an edge made up from $\mathbf{P}_1$ and $\mathbf{P}_2$ the normal direction of a potential SE contact is calculated as

$$\mathbf{n}^E = \frac{\overrightarrow{\mathbf{P}_1\mathbf{P}_s} - \left(\overrightarrow{\mathbf{P}_1\mathbf{P}_2}\cdot\overrightarrow{\mathbf{P}_1\mathbf{P}_s}\right)\dfrac{\overrightarrow{\mathbf{P}_1\mathbf{P}_2}}{\left|\overrightarrow{\mathbf{P}_1\mathbf{P}_2}\right|}}{\left|\overrightarrow{\mathbf{P}_1\mathbf{P}_s} - \left(\overrightarrow{\mathbf{P}_1\mathbf{P}_2}\cdot\overrightarrow{\mathbf{P}_1\mathbf{P}_s}\right)\dfrac{\overrightarrow{\mathbf{P}_1\mathbf{P}_2}}{\left|\overrightarrow{\mathbf{P}_1\mathbf{P}_2}\right|}\right|} \tag{43}$$

If $R - \left|\overrightarrow{\mathbf{P}_1\mathbf{P}_s} - \left(\overrightarrow{\mathbf{P}_1\mathbf{P}_2}\cdot\overrightarrow{\mathbf{P}_1\mathbf{P}_s}\right)\dfrac{\overrightarrow{\mathbf{P}_1\mathbf{P}_2}}{\left|\overrightarrow{\mathbf{P}_1\mathbf{P}_2}\right|}\right| > 0$ then the SE contact is further assessed. The potential contact point is calculated as

$$\mathbf{P}_4^{\mathrm{SE}} = \mathbf{P}_s - \overrightarrow{\mathbf{P}_1\mathbf{P}_s} + \left(\overrightarrow{\mathbf{P}_1\mathbf{P}_2}\cdot\overrightarrow{\mathbf{P}_1\mathbf{P}_s}\right)\frac{\overrightarrow{\mathbf{P}_1\mathbf{P}_2}}{\left|\overrightarrow{\mathbf{P}_1\mathbf{P}_2}\right|} \tag{44}$$

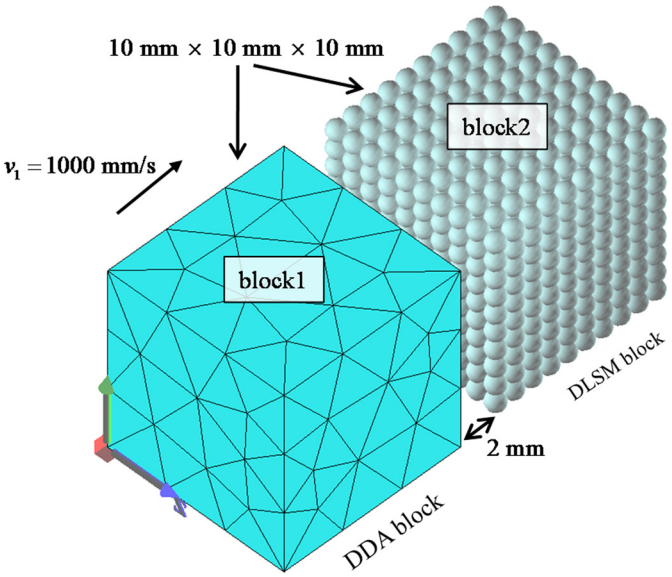

Fig. 6. Computational model of the two-box collision problem

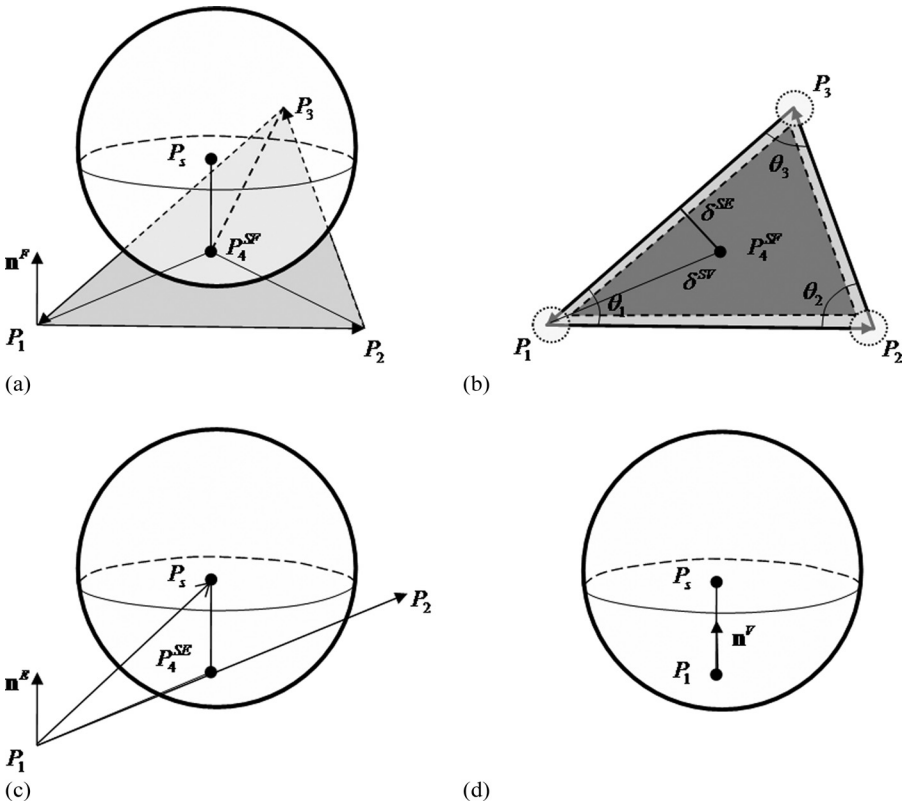

Fig. 5. Simplex 3D sphere-to-block contact scheme: (a) SF contact; (b) special conditions of SF contact; (c) SE contact; (d) SV contact

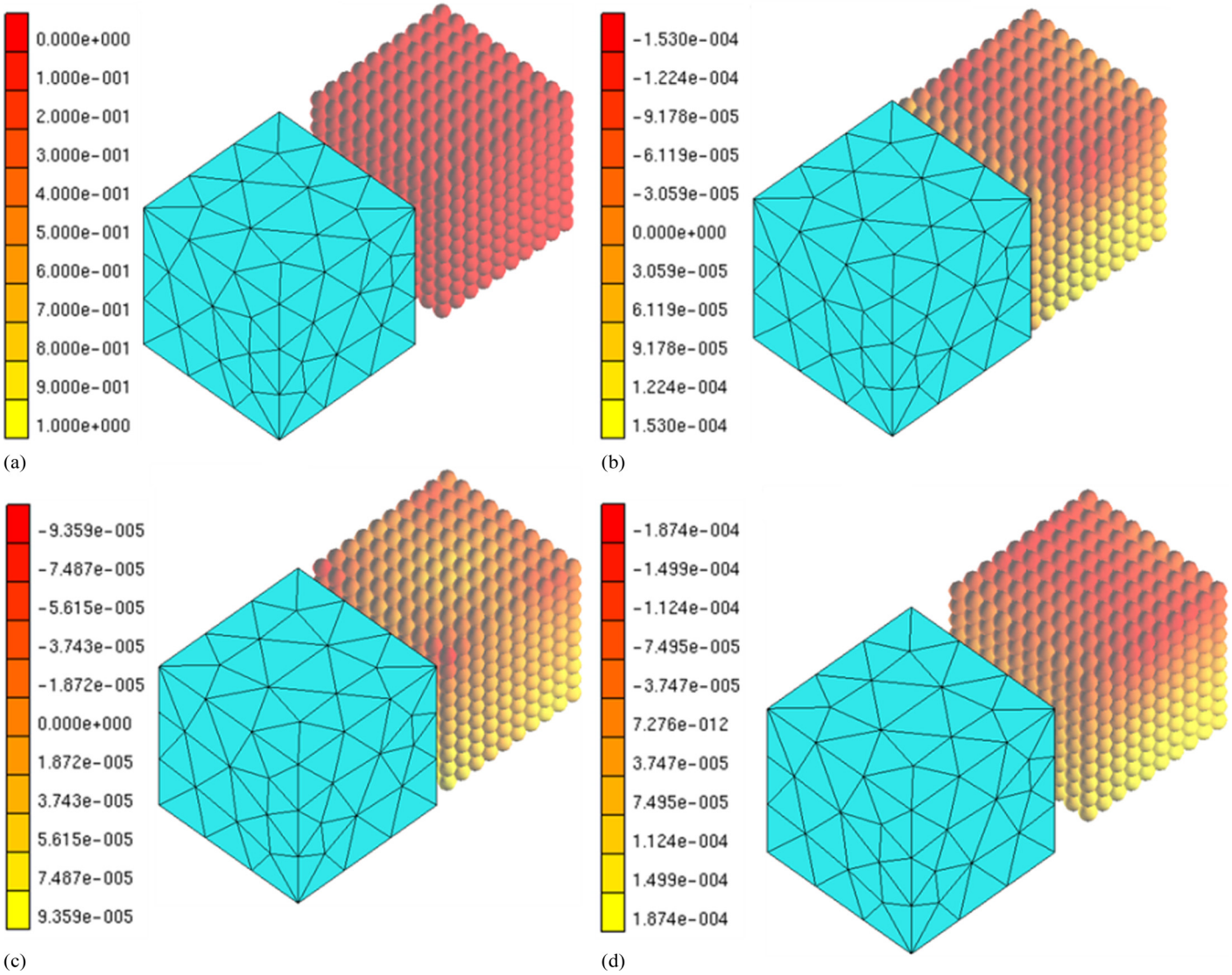

Fig. 7. Collision process between two boxes predicted by DDA-DLSM [Note: The contour refers to the displacement in the *Y*-direction (in millimeters)]: (a) $t = 0.00$ ms; (b) $t = 2.05$ ms; (c) $t = 2.85$ ms; (d) $t = 4.65$ ms

The potential contact point will be further assessed even further if it is inside the edge. If it is inside the edge then the contact overlap is calculated as

$$d^{\mathrm{sf}} = R - \left| \overrightarrow{\mathbf{P}_1\mathbf{P}_s} - \left(\overrightarrow{\mathbf{P}_1\mathbf{P}_2} \cdot \overrightarrow{\mathbf{P}_1\mathbf{P}_s} \right) \frac{\overrightarrow{\mathbf{P}_1\mathbf{P}_2}}{\left| \overrightarrow{\mathbf{P}_1\mathbf{P}_2} \right|} \right| \tag{45}$$

For an SE contact, as is similar for a SF contact, if the distance between the potential contact point and triangle vertex is smaller than the threshold value then the corresponding α must also be modified.

The SV contact can be dealt with easily. The contact normal and overlap can be obtained as

$$\mathbf{n}^V = \frac{\overrightarrow{\mathbf{P}_i\mathbf{P}_s}}{\left| \overrightarrow{\mathbf{P}_i\mathbf{P}_s} \right|} \tag{46}$$

$$d^{\mathrm{sf}} = R - |\overrightarrow{\mathbf{P}_i\mathbf{P}_s}| \tag{47}$$

An SV contact is only possible when $d^{\mathrm{sf}} > 0$. The sphere-block contact presented in this work only considers the normal interaction between DLSM and DDA. Shear contacts between a sphere and triangles is more complex and will be worked out in the future.

The time step for a coupled DDA-DLSM analysis is determined from the numerical stability requirement of DLSM because the time step selection of the implicit DDA is more flexible and can be large. In the following section a number of examples are conducted to verify the coupled DDA-DLSM, the contact treatment, and the numerical implementation.

Numerical Examples

Collision of Two Boxes

In this example, a collision problem will be solved using DDA-DLSM. The model configuration is shown in Fig. 6. There are two $10 \times 10 \times 10$-mm boxes, one represented by DDA and the other by DLSM. The gap between the two boxes is 2 mm. The elastic moduli of these two boxes are taken as 200 GPa and their Poisson's ratios

are taken to be 0.2563, representing a steel. The density of the DLSM box is taken as $\rho_2 = 7{,}900\,\mathrm{kg/m^3}$ and the density of the DDA box is taken as $\rho_1 = \chi\rho_2$. The DDA block is assigned with an initial velocity $v_1 = 1{,}000\,\mathrm{mm/s}$. According to the momentum and energy equilibrium of the two-box system the velocity of the DDA and DLSM boxes after collision v' can be obtained as

$$v_1' = \frac{1 - m_1/m_2}{1 + m_1/m_2} v_1 \tag{48}$$

$$v_2' = \frac{m_1(v_1 + v')}{m_2} \tag{49}$$

where m_1 and m_2 = masses of the DDA and DLSM boxes, respectively.

Fig. 7 shows the collision process predicted by DDA-DLSM when the two boxes have the same density (i.e., $\chi = 1.0$). It can be concluded that the coupling between DDA and DLSM is implemented correctly. There are no contacts between DDA and DLSM at the initial stage. Dynamic contacts are formed during the collision. The contour map of displacement along the y-direction of the DLSM box during the collision can be further used to check implementation of the simplex contact. The symmetrical square contact plane is represented as a group of triangles that do not have a symmetrical property (see Fig. 6). If the edge and vertex contact

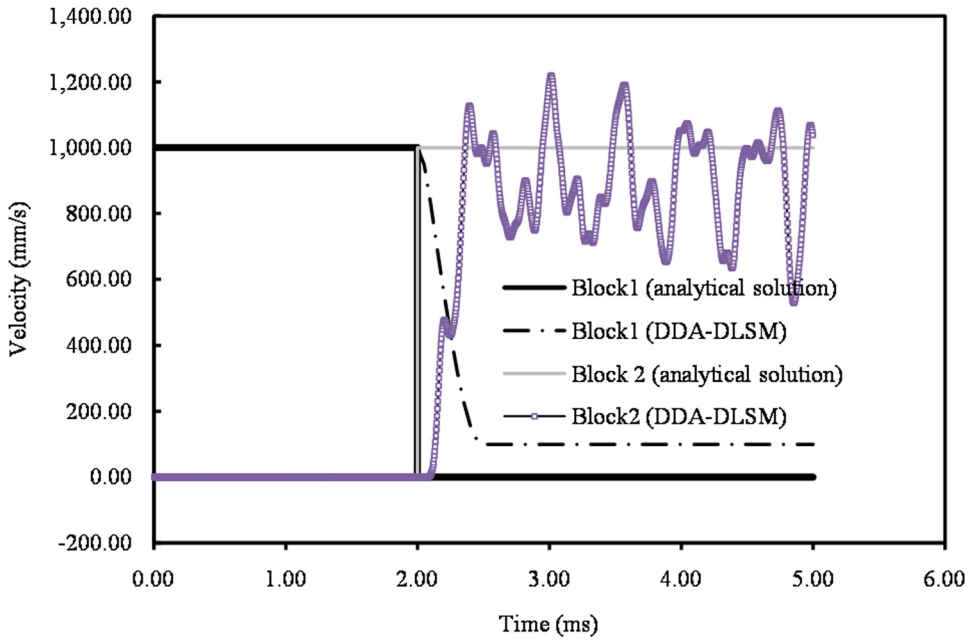

Fig. 8. Velocity histories of two boxes predicted by DDA-DLSM

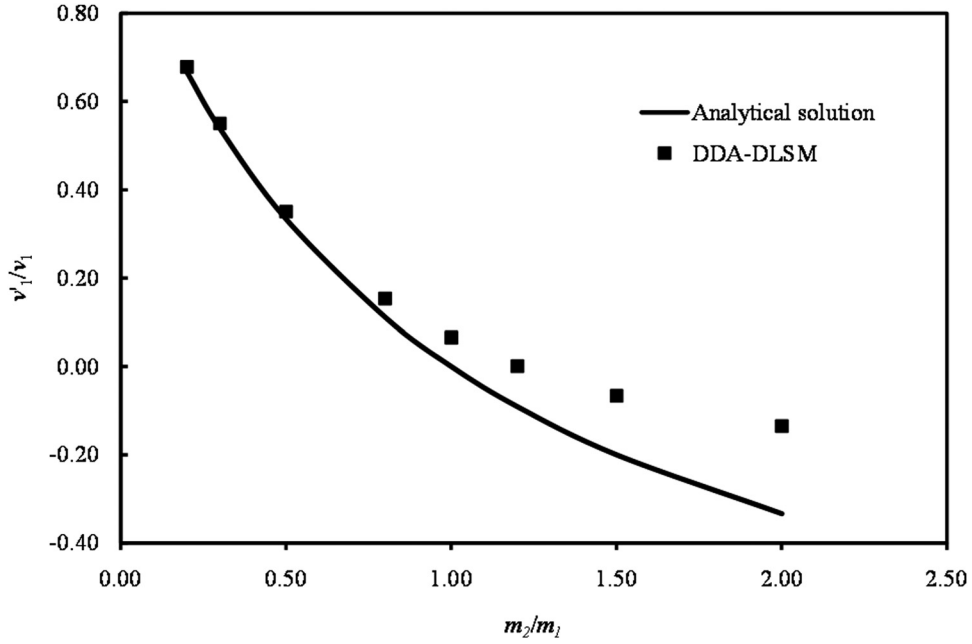

Fig. 9. Analytical and numerical results of the velocity exchange ratio (v_1'/v_1) and the mass ratio (m_2/m_1)

coefficients are not properly treated then the deformation would not be symmetrical, like that shown in Fig. 7. Therefore, because symmetry is clearly evident, the interaction between DDA and DLSM was handled properly by the proposed simplex sphere-block contact method.

The velocity histories of the DDA box and that of the center of the DLSM box are plotted in Fig. 8 for quantitative comparison with the analytical solution. General agreement is observed. The divergent and vibration of the numerical prediction is caused by the full 3D simulation of DDA-DLSM. Stress wave propagation and reflection happens within the DLSM box causing a vibration to be observed in the velocity history of the DLSM box.

To explore this problem further different densities for the DDA box are considered. The ratio between the after-collision velocity and the initial velocity of the DDA box is compared with the analytical prediction based on Eq. (48) (Fig. 9). When the mass of the impact box is small the numerically predicted velocity is close to the analytical solution. When the mass of the impact box is large the

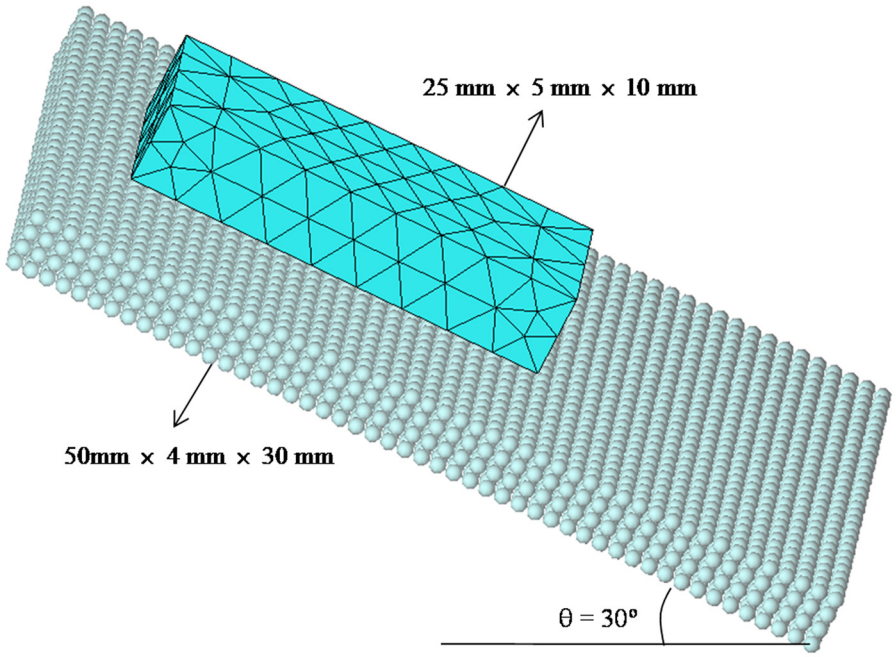

Fig. 10. Computational model of the sliding box problem

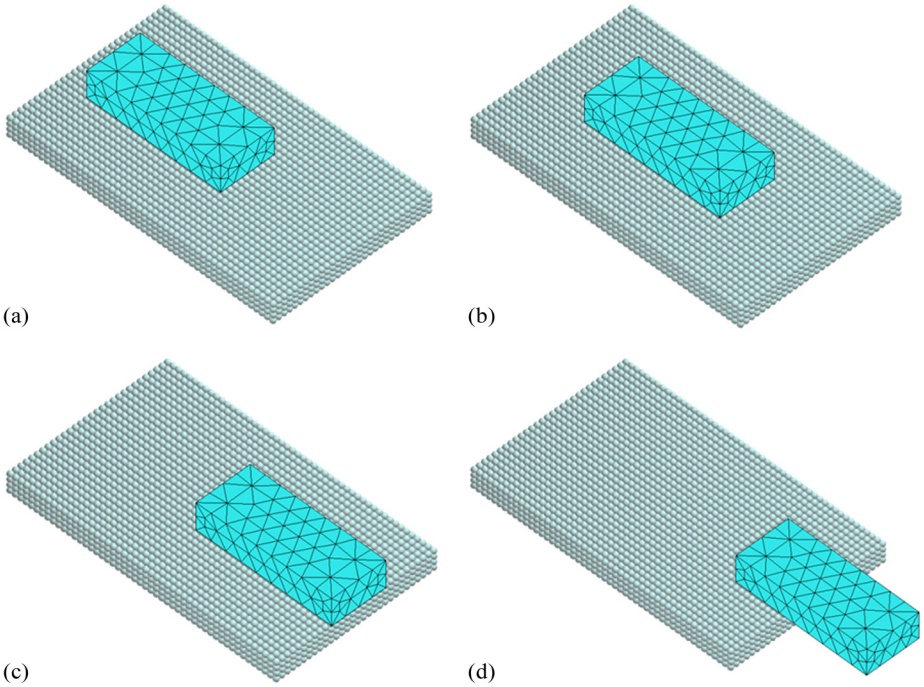

Fig. 11. Sliding process of the DDA box predicted by DDA-DLSM: (a) $t = 10$ ms; (b) $t = 50$ ms; (c) $t = 90$ ms; (d) $t = 120$ ms

numerical prediction deviates from the analytical solution. The reason is that when the mass is small the system is a DDA controlled system (the DLSM box can be viewed as a rigid wall and the DDA box as a semirigid body) close to the idealized system used to derive Eq. (48). On other hand, when the DDA block mass is large, the whole process is dominated by 3D stress wave propagation, and reflection within the DLSM box and Eq. (48) is unable to give a suitable predication. It is worth mentioning that different time steps were used in these simulations, and the results were the same.

This example has verified the coupling cycle and contact treatment of DDA-DLSM. However, for many problems, the contact between DDA and DLSM will change dynamically along the shear direction during simulation. In the following example a sliding box problem will be performed to illustrate how this can be dealt with.

Sliding Box

The model of a problem involving a box sliding on a table is shown in Fig. 10. The table is made up from DLSM particles and has the dimensions $50 \times 4 \times 30$ mm. The box is represented by DDA triangles and has the dimensions $25 \times 5 \times 10$ mm. The DDA box is placed just above the table. Because there is no shear contact applied in the coupled DDA-DLSM, the sliding distance of the DDA box can be written as

$$u^{\mathrm{sl}}(t) = \frac{1}{2} g \sin(\theta) t^2 \tag{50}$$

where t = sliding time; g = gravity acceleration (10 m/s^2); and θ = inclination angle of the table.

The particle size of the table is 1 mm and the model is made up of 600 particles. The material parameters of the two boxes are selected to be the same as steel: elastic modulus of 200 GPa, Poisson's ratio of 0.2563, and density of 7,900 kg/m^3. The simulation time is 0.15 s and the time step is 1×10^{-7} s. The total number of calculation cycles is 1.5 million. Therefore, this example can also check the numerical stability of DDA-DLSM during a long time simulation problem.

The sliding process predicted by DDA-DLSM is shown in Fig. 11. The DDA box is sliding under gravity and reaches the edge of the table as expected. The process involves dynamic contact detection between the table particles and the DDA triangles. This figure can confirm that the dynamic detection and treatment are implemented correctly. A comparison between the sliding distance predicted by DDA-DLSM and the analytical solution is plotted in Fig. 12. It shows that both stable and accurate results are obtained by DDA-DLSM.

This and the previous example verify that the contact coupling within DDA-DLSM has been done correctly. The two following examples involve rock penetration and rock cutting and will provide further verification of other implementation aspects.

Rock Penetration

A rock penetration test is a classical test used in the protective design of engineering structures. A high-speed impactor is sent to a rock specimen, which breaks up during impact and penetration. Experimental tests may be conducted to study the failure process of the rock (Seah et al. 2011) [Fig. 13(a)]. Seah et al. (2011) also conducted a FEM numerical simulation of the problem using a HJC-concrete model (involving 20 parameters including an erosion criterion). The FEM simulation result is shown in Fig. 13(b).

In this example DDA-DLSM is used to simulate a similar rock penetration test. As shown in Fig. 13(c) a steel impactor is assigned with an initial velocity of 200 m/s. It will impact the target. The material parameters of the steel are the same as in the previous section. The rock material properties are elastic modulus of 40 GPa, Poisson's ratio of 0.2, and density of 2,700 kg/m^3. The particle size adopted is 0.01 m. There is only one failure parameter, the ultimate tension deformation u_n^*, needed in the computational model. Fig. 13(c) shows the side view of the computational model. The front view is shown in Fig. 13(d). To investigate the influence of microstructure, two heterogeneous models are built [see Fig. 13(e and f)]. The first is a random two-phase model made by assigning different material properties to different particles randomly [see Fig. 13(e)]. The

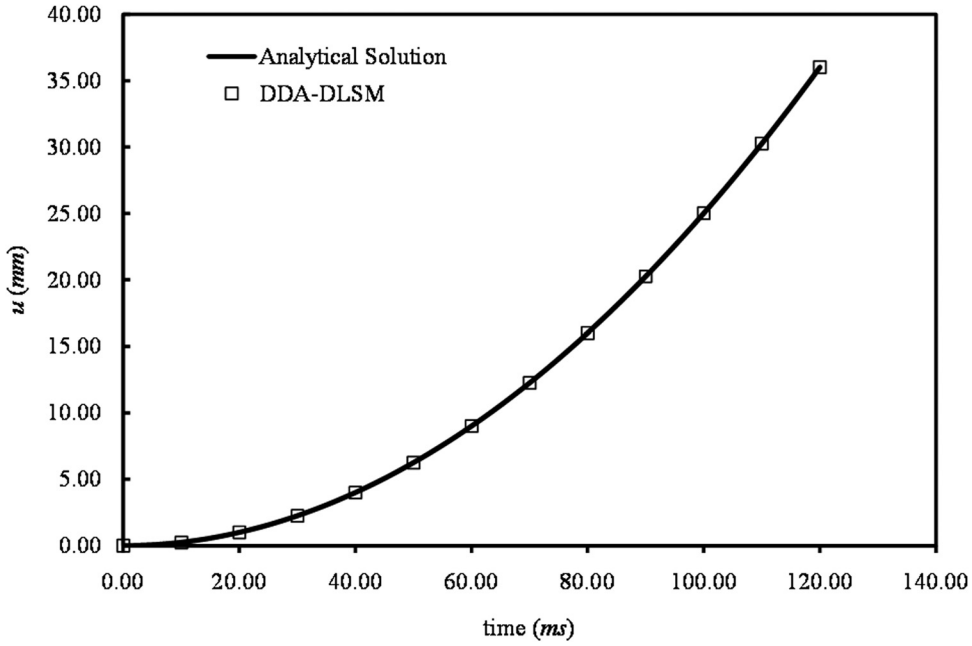

Fig. 12. Sliding distance predicted by DDA-DLSM and the analytical solution

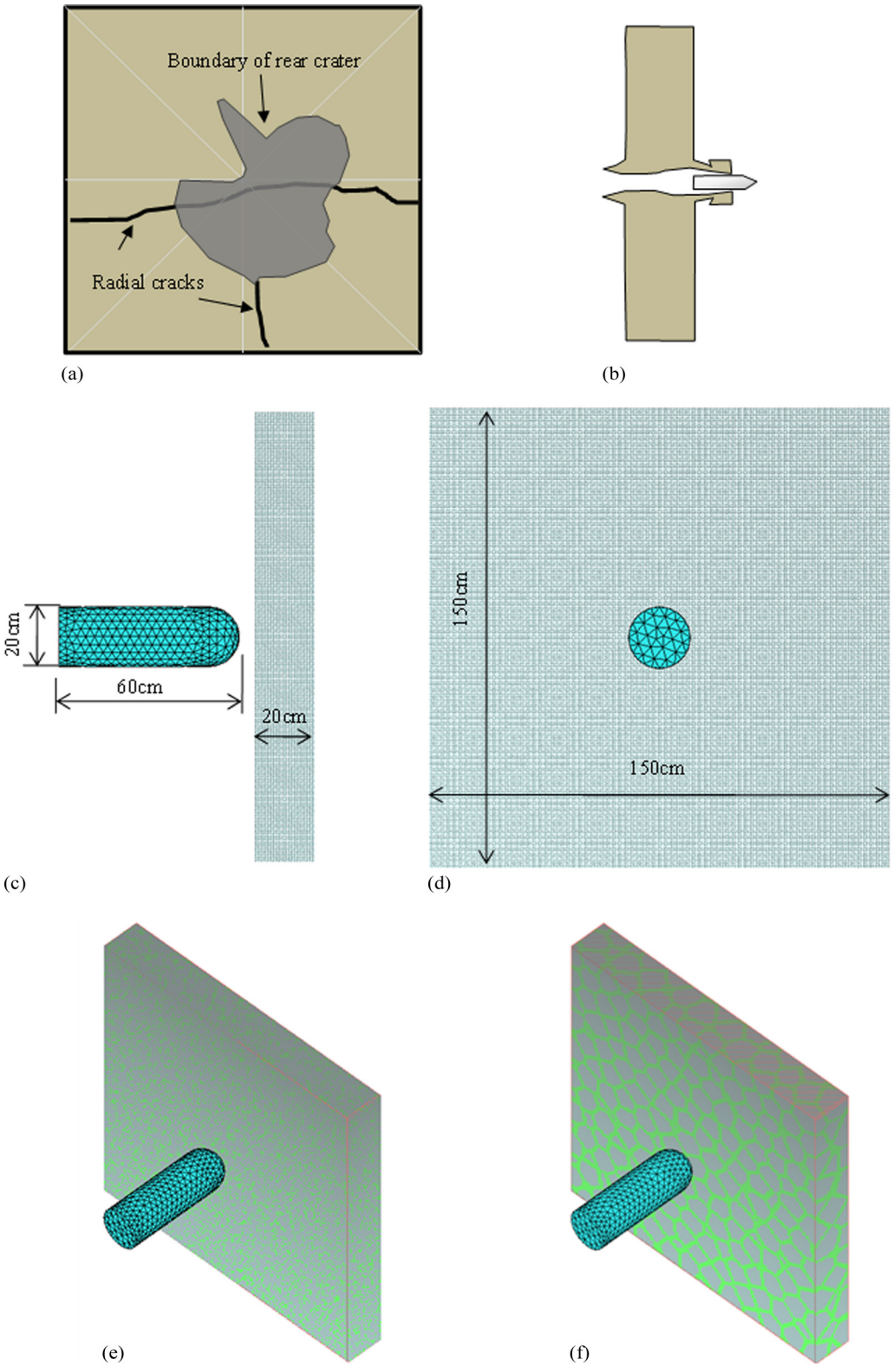

Fig. 13. Experimental and FEM simulation results of the rock penetration (data from Seah et al. 2011) and DDA-DLSM computational models for the problem: (a) experimental failure pattern (back) (data from Seah et al. 2011); (b) FEM simulation result (data from Seah et al. 2011); (c) side view; (d) front view; (e) random model; (f) Voronoi model

second is a Voronoi-based model. The surface of a Voronoi cell is assigned material parameters of the base material. The base material made up about 80 and 20% for the first (random) and second (Voronoi) models, respectively.

A parameter study on u_n^* is conducted first using the homogenous model. Fig. 14(a) shows the failure pattern when u_n^* = 0.0001 m. The failure zone of the rock specimen's back takes the shape of a four-cornered star and is different from the experimental

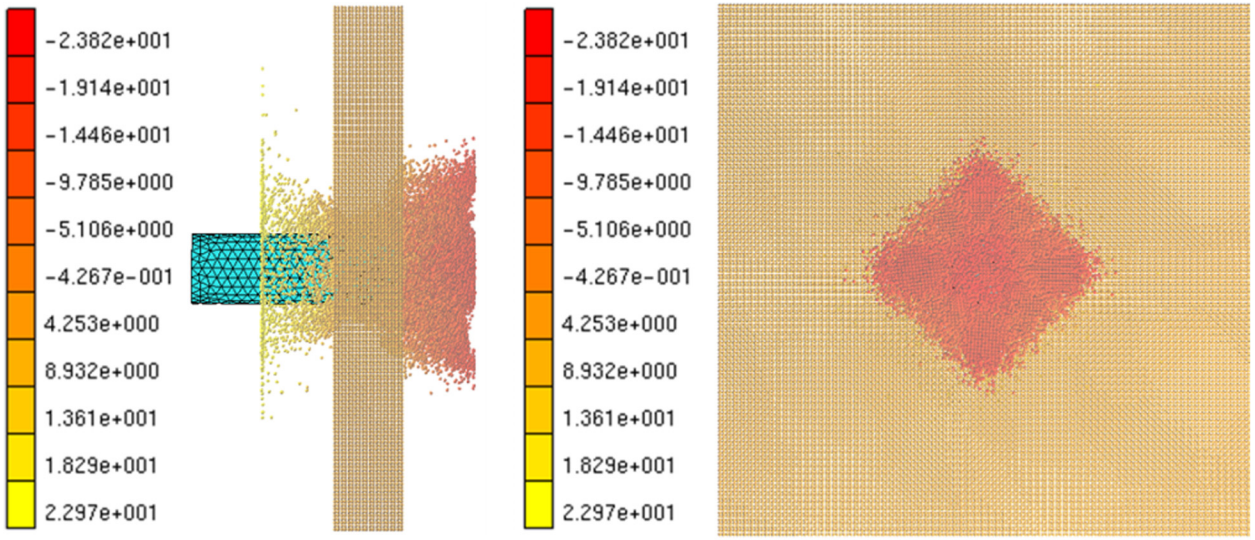

(a)

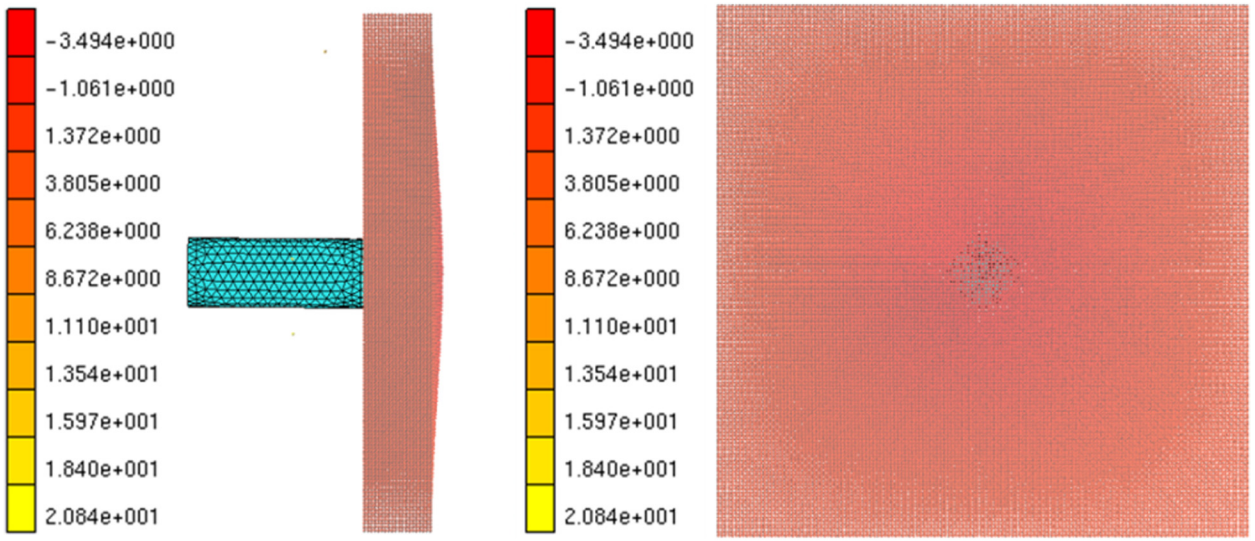

(b)

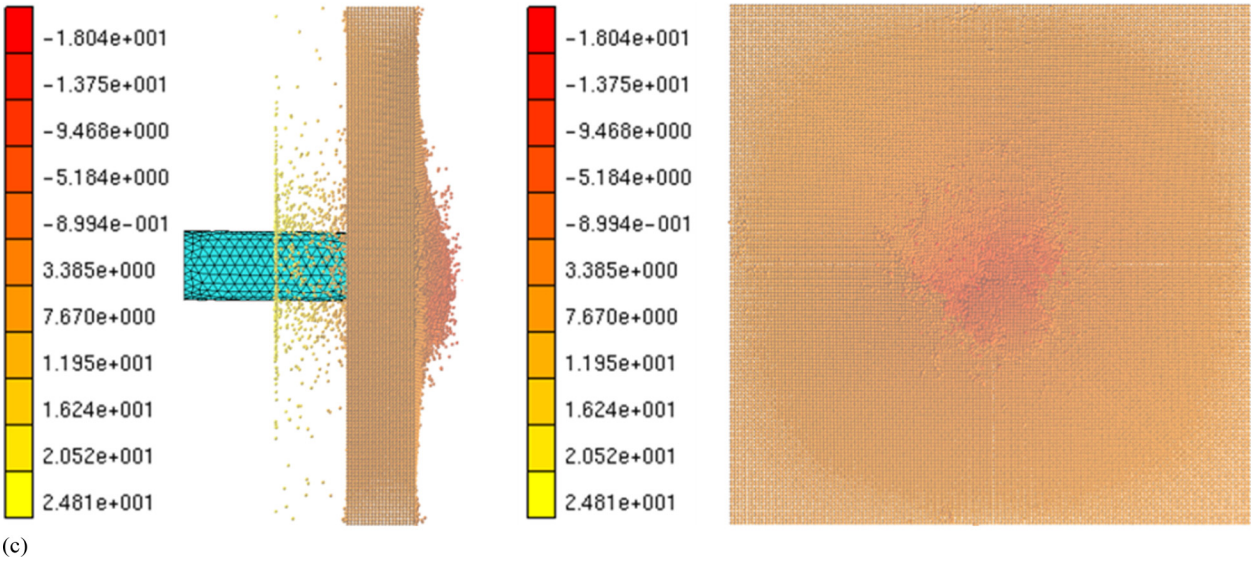

(c)

Fig. 14. Failure patterns of the rock specimen predicted by DDA-DLSM: (a) homogenous model ($u_n^* = 0.0001$ m); (b) homogenous model ($u_n^* = 0.0010$ m); (c) random model ($u_{n1}^* = 0.0001$ m, $u_{n2}^* = 0.0010$ m); (d) Voronoi model ($u_{n1}^* = 0.0001$ m, $u_{n2}^* = 0.0010$ m)

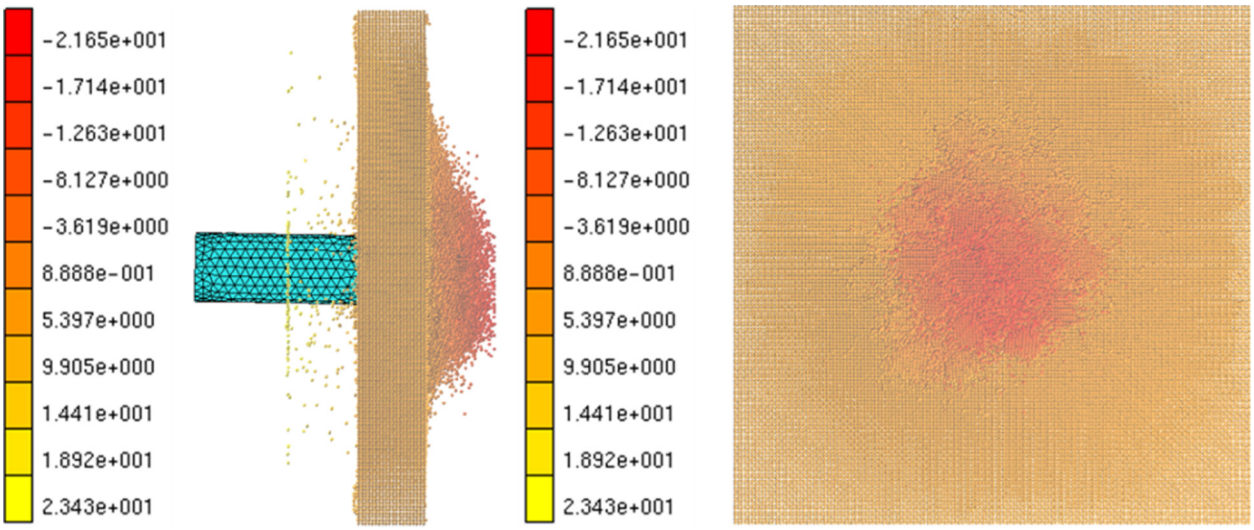

(d)

Fig. 14. (*Continued.*)

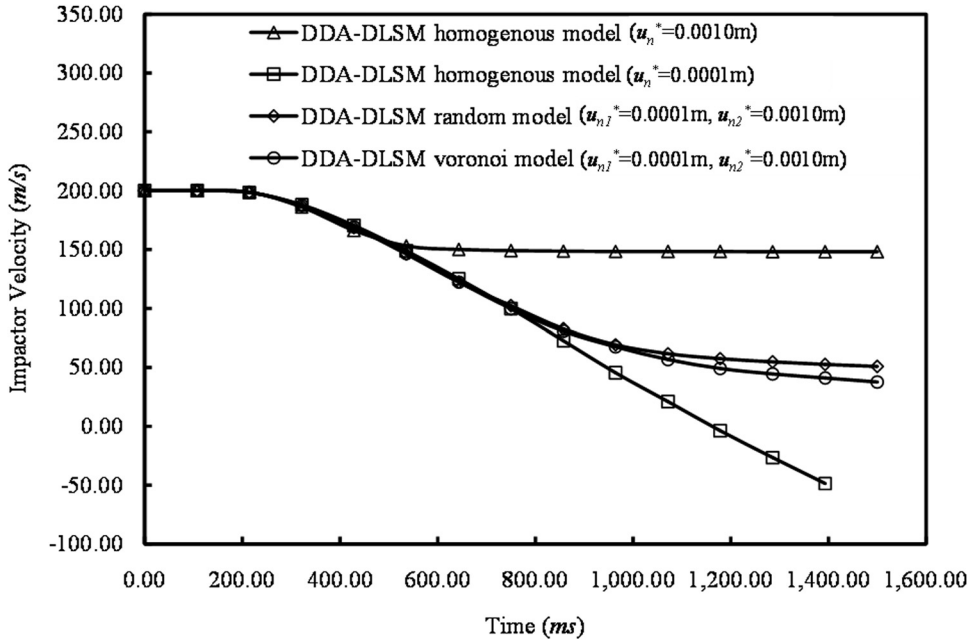

Fig. 15. Histories of the impactor's velocity predicted by DDA-DLSM

observation [see Fig. 13(a)]. When the strength parameter u_n^* is set as 0.0010 m, as shown in Fig. 14(b), no apparent failure is observed although a bulking shell forms at the back. These two material parameters ($u_{n1}^* = 0.0001$ m and $u_{n2}^* = 0.0010$ m) are used to represent the base material and enriched material within the heterogeneous random and Voronoi models. As shown in Figs. 14(c and d) the failure patterns of the heterogeneous models are similar to the experimental observation. Compared with the FEM results [Fig. 13(b)] the Voronoi-based heterogeneous model using DDA-DLSM can reproduce a more realistic failure pattern. The reason might be that the dynamic failure of the rock specimen under impact penetration is mainly controlled by the local tensional failure and the dynamic contacts between fragments.

The beauty of discontinuum-based modeling is that experimental results can be fitted using a relatively simple mechanical model. Once this fitting is done the influence of a range of geometric factors, which are difficult to study experimentally, can be investigated numerically. For example, the two heterogeneous models shown in Figs. 13(e and f) represent models with two different portions of enriched material and different topological distributions. Through numerical simulation the influence of topological distribution of the enrichment and portion of the enrichment can be studied.

Fig. 15 shows the velocity histories of the impactor. For the homogenous model made of base material only the impactor would penetrate the rock specimen completely, and the residual velocity is about 150 m/s. For the homogenous model made of enriched material only the impactor will be reflected at a velocity of about −50 m/s. The outputs of random and Voronoi heterogeneous models are in between the two homogenous model outputs, and the residual velocity is about 50 m/s. The random heterogeneous model

has around 20% enrichment material, whereas 80% enrichment material is used for the Voronoi model. However, the performance of the random model is slightly better than the Voronoi model. This indicates that the topological distribution of enrichment has more weight than the portion each material makes up within the enrichment. Also, it seems the random distribution of enrichment material is more crucial than simply increasing its portion to achieve realistic model outputs.

In this example, damping coefficients of DDA and DLSM are set to be zero due to the very short simulation time considered (less than 2 s). Overall, the DDA-DLSM is able to capture the rock penetration process reasonably. Nevertheless, it still needs further improvements and developments, particularly in its ability to model shear failure, plastic deformation, damage accumulation, and energy dissipation caused by viscous damping (Jiang et al. 2013).

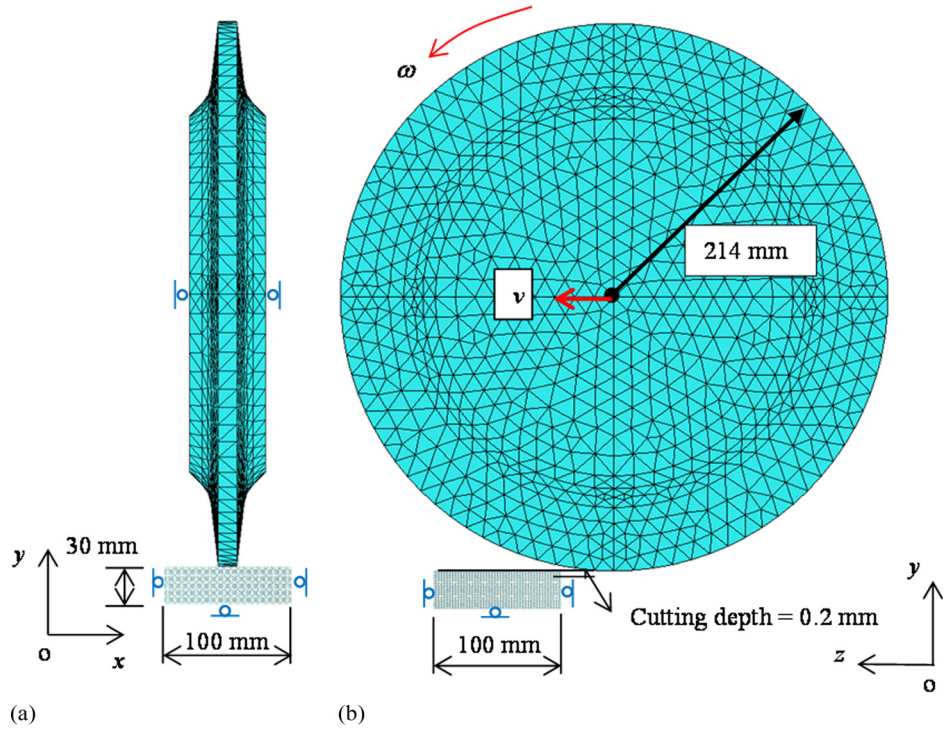

Fig. 16. Computational model of the TBM cutting problem: (a) front view; (b) side view

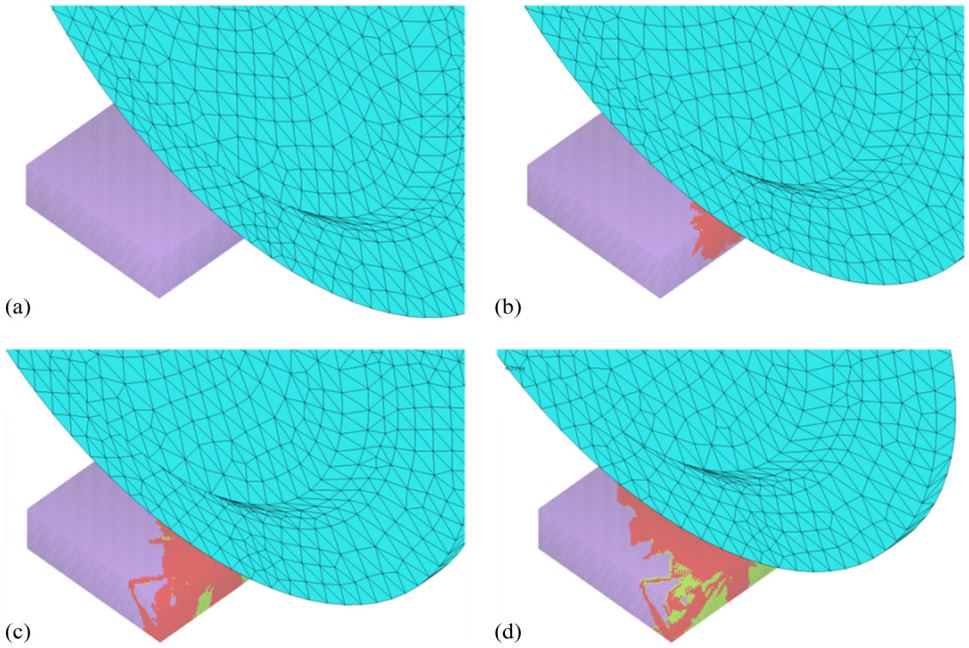

Fig. 17. TBM cutting process simulated by DDA-DLSM: (a) $t = 0.1$ ms; (b) $t = 0.6$ ms; (c) $t = 1.4$ ms; (d) $t = 2.0$ ms

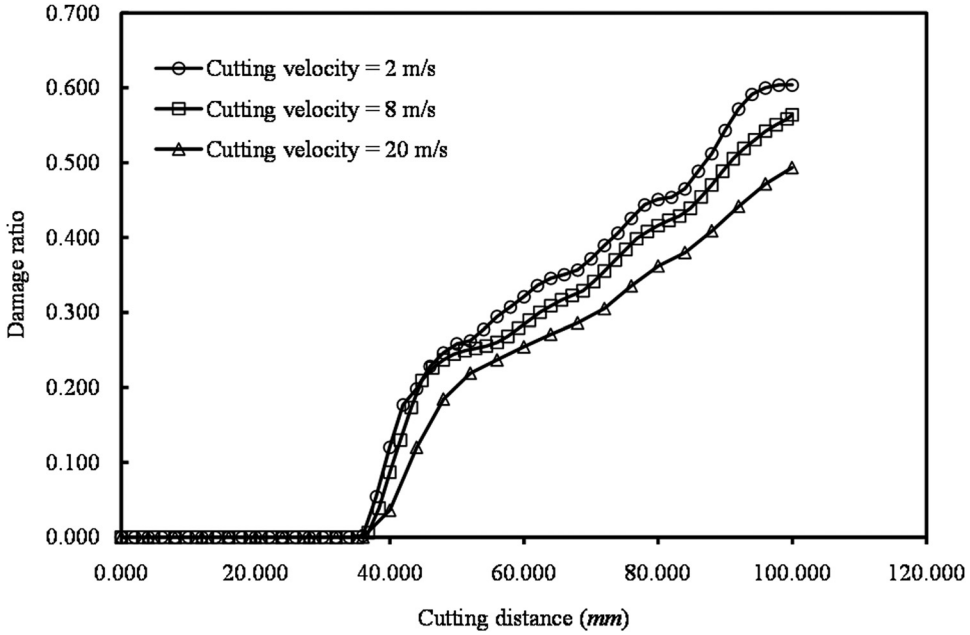

Fig. 18. Influence of cutting velocity on damage ratio during TBM cutting

TBM Rock Cutting

In this example a TBM rock cutting problem is simulated. A full 3D model of a TBM cutter is used (Fig. 16). Unlike the FEM simulation of Cho et al. (2010) only the surface triangles for the cutter are adopted in this study. Moreover, there are only 7 DOFs for the cutter in DDA-DLSM. The radius of the cutter is 214 mm, thickness is 80 mm, and the width of the cutter head is 14 mm. The rock block's dimension is $100 \times 100 \times 30$ mm, which is made up from 300,000 particles with a diameter of 1 mm. The material properties of the cutter are elastic modulus of 120 GPa and Poisson's ratio of 0.25. The density of the steel cutter and rock are 7,900 kg/m^3 and 2,600 kg/m^3, respectively, which are scaled 1,000 times in the simulation to allow a large time step (~33 times) to be used as a preliminary solution to overcome the computational limitation of our current program. It should be mentioned that this increase of density will cause the change of inertia force and might influence the simulation results. A parallel code will be developed to tackle this problem in future work. The ultimate deformation of the normal and shear springs are taken to be 0.00015 and 0.001 mm, respectively. The boundary conditions applied to the block are free surfaces except the top one, which is fixed in its normal direction. The TBM cutter will move along the z-direction while also rotating around its central axis. The angular velocity applied is $\omega = v/R$, where v = cutting velocity; and R = radius of the TBM cutter.

The failure process of the rock specimen under TBM cutting is shown in Fig. 17. The damage zone expands in the direction of movement of the TBM cutter. The typical branch fractured zone is observed, which is similar with the experimental observation of Cho et al. (2010).

In this example the influence of cutting velocity is studied to highlight the ability of DDA-DLSM to model rock cutting problems. The damage volume ratio versus cutting distance under different cutting velocities is shown in Fig. 18. It can be seen that slow cutting results in a more damaged specimen. Fast cutting will results in less damage. This is in agreement with classic experimental observations from rock dynamic testing. For example, the strength and fracture toughness of rock are usually higher and the extent of damage usually lower under higher strain/loading rates (Dai et al. 2010). Through numerical simulation this can also be observed, in particular in a TBM rock cutting process. This type of numerical simulation may be used to optimize the operation speed and energy efficiency of rock cutting.

Conclusions

A coupled DDA-DLSM approach is developed for rock cutting and rock penetration problems. The cutter is modeled as a surface of tessellated triangles using the simplex concept of DDA. The motion of the cutter/impactor is further described by the system equation of DDA. The rock specimen is modeled as a group of particles linked through springs. A coupling procedure with a 3D contact method is developed to integrate DLSM and DDA. By using a number of numerical examples the correctness of the proposed coupling technique and implementation of DDA-DLSM are verified. Results indicate that DDA-DLSM is a promising tool for studying and optimizing rock cutting and rock penetration problems. Further research will focus on more advanced constitutive model development for DLSM and more complete contact treatment between DLS M and DDA.

References

Beyabanaki, S. A. R., and Bagtzoglou, A. C. (2015). "Sphere-boundary edge and sphere-boundary corner contacts model in DDA for simulating particulate media in 3-D." *Geomech. Geoeng.*, 10(2), 83–94.

Beyabanaki, S. A. R., Jafari, A., and Yeung, M. R. (2010). "High-order three-dimensional discontinuous deformation analysis (3-D DDA)." *Int. J. Numer. Methods Biomed. Eng.*, 26(2), 1522–1547.

Cho, J. W., Jeon, S., Yu, S. H., and Chang, S. H. (2010). "Optimum spacing of TBM disc cutters: A numerical simulation using the three-dimensional dynamic fracturing method." *Tunnelling Underground Space Technol.*, 25(3), 230–244.

Dai, F., Xia, K. W., and Tang, L. Z. (2010). "Rate dependence of the flexural tensile strength of Laurentian granite." *Int. J. Rock Mech. Min. Sci.*, 47(3), 469–475.

Detournay, E., Richard, T., and Shepherd, M. (2008). "Drilling response of drag bits: theory and experiment." *Int. J. Rock Mech. Min. Sci.*, 45(8), 1347–1360.

Glowka, D. (1989). "Use of single-cutter data in the analysis of PDC bit designs: part 1-development of a PDC cutting force model." *J. Pet. Technol.*, 41(8), 797–799.

Gong, Q. M., Jiao, Y. Y., and Zhao, J. (2006). "Numerical modelling of the effects of joint spacing on rock fragmentation by TBM cutters." *Tunnelling Underground Space Technol.*, 21(1), 46–55.

Guo, H. (1990). "Rock cutting using fracture mechanics principles." Ph.D. thesis, Univ. of Wollongong, New South Wales, Australia.

Hansson, H., and Skoglund, P. (2002). "Simulation of concrete penetration in 2D and 3D with the RHT material model." *Tech. Rep.*, Swedish Deference Research Agency, Stockholm, Sweden.

He, L., An, X. M., and Zhao, Z. Y. (2014). "Development of contact algorithm for three-dimensional numerical manifold method." *Int. J. Numer. Methods Eng.*, 97(6), 423–453.

Hughes, G. (1984). "Hard missile impact on reinforced concrete." *Nucl. Eng. Des.*, 77(1), 23–35.

Ingraffea, A. R. (1987). "Theory of crack initiation and propagation in rock." *Fracture mechanics of rock*, B. K. Atkinson, ed., Academic Press, London, 101–107.

Jiang, Q. H., Chen, Y., Zhou, C. B., and Yeung, M. R. (2013). "Kinetic energy dissipation and convergence criterion of discontinuous deformations analysis (DDA) for geotechnical engineering." *Rock Mech. Rock Eng.*, 46(6), 1443–1460.

Jiang, Q. H., and Yeung, M. R. (2004). "A model of point-to-face contact for three-dimensional discontinuous deformation analysis." *Rock Mech. Rock Eng.*, 37(2), 95–116.

Jiang, Q. H., Zhou, C. B., and Li, D. Q. (2009). "A three-dimensional numerical manifold method based on tetrahedral meshes." *Comput. Struct.*, 87(13–14), 880–889.

Jing, L. (2003). "A review techniques, advances and outstanding issues in numerical modelling for rock mechanics and rock engineering." *Int. J. Rock Mech. Min. Sci.*, 40(3), 283–353.

Kaitkay, P., and Lei, S. (2005). "Experimental study of rock cutting under external hydrostatic pressure." *J. Mater. Process. Technol.*, 159(2), 206–213.

Kusano, N., Aoyagi, T., Aizawa, J., Ueno, H., Morikawa, H., and Kobayashi, N. (1992). "Impulsive local damage analyses of concrete structure by the distinct element method." *Nucl. Eng. Des.*, 138(1), 105–110.

Li, J., Ma, G., and Yu, M. (2008). "Penetration analysis for geo-material based on unified strength criterion." *Int. J. Impact Eng.*, 35(10), 1154–1163.

Li, Q. M., and Chen, X. W. (2003). "Dimensionless formulae for penetration depth of concrete target impacted by a non-deformable projectile." *Int. J. Impact Eng.*, 28(1), 93–116.

Liu, H. Y., Kou, S. Q., and Lindqvist, P. A. (2002). "Numerical simulation of the fracture process in cutting heterogeneous brittle material." *Int. J. Numer. Anal. Methods Geomech.*, 26(13), 1253–1278.

Ma, H. S., Yin, L. J., and Ji, H. G. (2011). "Numerical study of the effect of confining stress on rock fragmentation by TBM cutters." *Int. J. Rock. Mech. Min. Sci.*, 48(6), 1021–1033.

Mahabadi, O., Lisjak, A., Munjiza, A., and Grasselli, G. (2012). "Y-Geo: New combined finite-discrete element numerical code for geomechanical applications." *Int. J. Geomech.*, 10.1061/(ASCE)GM.1943-5622.0000216, 676–688.

Moon, T., and Oh, J. (2012). "A study of optimal rock-cutting conditions for hard rock TBM using the discrete element method." *Rock Mech. Rock Eng.*, 45(5), 837–849.

Munjiza, A. (2004). *The combined finite-discrete element method*, Wiley, Hoboken, NJ.

Nishimatsu, Y. (1972). "The mechanics of rock cutting." *Int. J. Rock. Mech. Min. Sci. Geomech. Abstr.*, 9(2), 261–270.

Onate, E., and Rojek, J. (2004). "Combination of discrete element and finite element methods for dynamic analysis of geomechanics problems." *Comput. Methods Appl. Mech. Eng.*, 193, 3087–3128.

Seah, C. C., Bervik, T., Remseth, S., and Pan, T.-C. (2011). "Penetration and perforation of rock targets by hard projectiles." *Advances in rock dynamics and applications*, Jian Zhao, ed., CRC Press, Boca Raton, FL.

Shi, G. H., and Goodman, R. E. (1985). "Two dimensional discontinuous deformation analysis." *Int. J. Num. Anal. Mech. Geomech.*, 9(6), 541–556.

Shi, G. H. (1988). "Discontinuous deformation analysis: A new numerical model for the statics and dynamics of block systems." Ph.D. thesis, Univ. of California, Berkeley, CA.

Shiu, W., Donze, F. V., and Daudeville, L. (2009). "Discrete element modelling of missile impacts on a reinforced concrete target." *Int. J. Comput. Appl. Technol.*, 34(1), 33–41.

Yeung, M. R., Jiang, Q. H., and Sun, N. (2007). "A model of edge-to-edge contact for three-dimensional discontinuous deformation analysis." *Comput. Geotech.*, 34(3), 175–186.

Yin, L. J., Gong, Q. M., and Zhao, J. (2014). "Study on rock mass boreability by TBM penetration test under different in situ stress conditions." *Tunnelling Underground Space Technol.*, 43, 413–425.

Zhao, G. F., Fang, J. N., Sun, L., and Zhao, J. (2013). "Parallelization of the distinct lattice spring model." *Int. J. Numer. Anal .Methods Geomech.*, 37(1), 51–74.

Zhao, G. F., Fang, J., and Zhao, J. (2011). "A 3D distinct lattice spring model for elasticity and dynamic failure." *Int. J. Numer. Anal. Methods Geomech.*, 35(8), 859–885.

Zhao, S. L. (2000). "Development of three-dimensional spherical discontinuous deformation analysis for granular materials." Ph.D. thesis, North Carolina State Univ., Raleigh, NC.

Zhou, Y. (2009). "Simulation of high-velocity penetration for rigid projectile into plain concrete target using discrete element method." M.Sc. thesis, Virginia Polytechnic Institute and State Univ., Blacksburg, VA.

Zhou, Y. N. (2013). "Numerical modeling of rock drilling with finite elements." Ph.D. thesis, Univ. of Pittsburgh, Pittsburgh.